

IEEE COPYRIGHT NOTICE

©2020 IEEE. Personal use of this material is permitted. Permission from IEEE must be obtained for all other uses, in any current or future media, including reprinting/republishing this material for advertising or promotional purposes, creating new collective works, for resale or redistribution to servers or lists, or reuse of any copyrighted component of this work in other works.

Accepted to be published in: Proceedings of the 2020 IEEE International Symposium on Hardware Oriented Security and Trust (HOST), December 6-9, 2020, San Jose, CA, USA

Encoding Power Traces as Images for Efficient Side-Channel Analysis

Benjamin Hettwer^{*†}, Tobias Horn[‡], Stefan Gehrer[§], Tim Güneysu[†]

^{*}Robert Bosch GmbH, Corporate Sector Research, Renningen, Germany

[†]Horst Görtz Institute for IT-Security, Ruhr University Bochum, Germany

[‡]Esslingen University of Applied Sciences, Esslingen, Germany

[§]Robert Bosch LLC, Corporate Sector Research, Pittsburgh, USA

Email: benjamin.hettwer@de.bosch.com, tohoit06@hs-esslingen.de, stefan.gehrer@bosch.com,
tim.gueneysu@rub.de

Abstract—Side-Channel Attacks (SCAs) are a powerful method to attack implementations of cryptographic algorithms. State-of-the-art techniques such as template attacks and stochastic models usually require a lot of manual preprocessing and feature extraction by the attacker. Deep Learning (DL) methods have been introduced to simplify SCAs and simultaneously lowering the amount of required side-channel traces for a successful attack. However, the general success of DL is largely driven by their capability to classify images, a field in which they easily outperform humans.

In this paper, we present a novel technique to interpret 1D traces as 2D images. We show and compare several techniques to transform power traces into images, and apply these on different implementations of the Advanced Encryption Standard (AES). By allowing the neural network to interpret the trace as an image, we are able to significantly reduce the number of required attack traces for a correct key guess. We also demonstrate that the attack efficiency can be improved by using multiple 2D images in the depth channel as an input. Furthermore, by applying image-based data augmentation, we show how the number of profiling traces is reduced by a factor of 50 while simultaneously enhancing the attack performance. This is a crucial improvement, as the amount of traces that can be recorded by an attacker is often very limited in real-life applications.

Index Terms—Side-channel attacks (SCAs), Deep Learning (DL), AES, Convolutional Neural Network (CNNs).

I. INTRODUCTION

Since the advent of Side-Channel Attacks (SCAs) by Kocher et al. in 1996 [1], the topic has become a serious threat for security devices and is extensively investigated in research and industry. SCAs take advantage of information leakages through timing, power consumption or Electromagnetic (EM) emanations to extract secret parameters from cryptographic algorithms implemented in software or hardware. Numerous attack methods have been proposed in literature to analyze side-channel leakages. These can be divided into two major categories: Non-profiled and profiled SCAs. Techniques such as Correlation Power Analysis (CPA) [2] or Mutual Information Analysis (MIA) [3] belong to the non-profiled class and aim to recover cryptographic keys by using statistical calculations between real power measurements and a hypothesis of the leakage behaviour of the device under attack. In profiled SCAs, the adversary performs an additional profiling

step with an open copy of the target device ahead of the actual attack using Gaussian templates [4], stochastic attacks [5], or machine learning methods [6].

Another path of work dealing with Deep Learning (DL)-based profiled side-channel analysis has been introduced by Maghrebi et al. in 2016 [7]. Several publications showed that especially Convolutional Neural Networks (CNNs) are able to outperform classic key recovery techniques (see, e.g., [8] [9] [10] for an incomplete list). CNNs are special types of DL models that were originally proposed for image recognition tasks [11]. They exploit local connection patterns in the input data through receptive fields and weight sharing, and are - to some degree - shift, scale, and distortion invariant. State-of-the-art CNN architectures for image classification like VGG have been winning the ImageNet Large Scale Visual Recognition Challenge (ILSVRC) since 2012, partly showing above human-level performance. In the context of SCAs, CNNs were mainly applied on the raw, one-dimensional side-channel traces. However, there are several ways to transform 1D data structures (like side-channel traces) to 2D images in order to enable visual learning techniques to recognize patterns in time series data. Hatami et al., e.g., proposed Recurrence Plots (RPs) to transform time series into 2D texture images [12]. Audio or sound classification can be performed with spectrograms in order to identify features in the time-frequency domain [13]. Wang and Oates introduced Gramian Angular Fields (GAFs) and Markov Transition Fields (MTFs) to encode time series as images and achieved state-of-the-art results on 20 different data sets [14].

Motivated by the success of CNNs in computer vision, this paper investigates the performance of profiled SCAs in 2D space. We encode power traces from four different data sets as images using GAF, MTF, RPs and spectrograms, and apply them to a 2D CNN in order to extract secret key bytes from cryptographic implementations. While there are notable differences between the methods, our experiments show that 2D-based attacks can be more powerful than their equivalents in 1D space. This holds also in case the traces are preprocessed with state-of-the-art 1D transformations such as Singular Spectrum Analysis (SSA) [15]. We furthermore

demonstrate how the performance of the CNN is further enhanced by combining different 2D representations of a trace into a single image as illustrated in Fig. 1. Finally, we explore image-based data augmentation to boost the robustness of our CNN model and report valid parameter settings for all transformation techniques.

The remaining structure of the paper is as follows: In Section II, we give an overview about related work. In Section III, we shortly recap profiled SCAs and introduce 2D CNNs. In Section IV, we present several techniques to transform time series to images and apply them to power traces. In Section V, we evaluate our approach by attacking unprotected and protected AES implementations. The last section summarizes the paper and gives insights on possible future work.

II. RELATED WORK

There have been numerous tools and techniques proposed in literature that deal with the preprocessing of side-channel traces to increase the power of SCAs. They can be grouped in the following categories:

A. Denoising

Techniques to improve the Signal-to-Noise Ratio (SNR) range from simple trace averaging to advanced filtering using Kalman and Wiener filters [16], or the forth-order cumulant to remove Gaussian noise [17]. Noise reduction in the frequency domain is also widely used in practice, e.g., wavelet-based methods [18], Hilbert transform [19] and SSA [15]. Maghrebi et al. recently proposed Independent Component Analysis, a technique for blind source separation, to denoise side-channel measurements and could show a significant SNR gain [20]. The methods investigated in this paper are not explicitly designed to decrease the level of noise in time series, but can be easily combined with them before the transformation in the 2D space is done.

B. Dimensionality Reduction and POI Selection

Identifying Points of Interest (POIs) or features in side-channel traces has been traditionally studied in the context of Template Attacks (TAs), in order to reduce the computational overhead during calculation of the covariance matrices. In particular, Difference of Means (DOM) [4], Sum Of Squared pairwise T-differences (SOST), Sum Of Squared Differences (SOSD) [21], and Principal Component Analysis (PCA) [22] have been proposed for that purpose. Another common strategy for POIs selection and dimensionality reduction is based on Pearson correlation, whereby the importance of sample points is measured by the correlation coefficient of the actual power consumption and some key-dependent target intermediate value [23].

C. Dataset Augmentation

Deep Neural Networks (DNNs) usually require a large amount of training data in order to learn effectively. Since generating more data is often too expensive or not possible at all, fake data can be created and added to the training

set which is referred to as dataset augmentation [24]. It has been particularly effective in object recognition tasks, where images are, e.g., flipped, rotated or cropped to boost the performance of the classifier [25]. Cagli et al. investigated data augmentation in the context of SCAs to defeat jitter-based countermeasures by artificially distorting traces [8]. To this end, shifting deformations (simulates random delay) and add-remove deformations (simulates clock jitter) were applied to the traces of different training sets. Pu et al. furthermore introduced a lazy validation method to find an appropriate range of which the traces can be shifted horizontally [26]. Recently, Kim et al. proposed to add Gaussian noise to the input during training in order to improve the attack performance [10]. In this work, we apply several data augmentation techniques to 2D representations of side-channel traces and compare them with the aforementioned methods from the 1D domain.

III. PRELIMINARIES

A. Profiled Side-Channel Attacks

Profiled attacks are considered as the most powerful type of SCAs and are composed of two phases: a *profiling* (or training) phase, and an *attack* phase (inference in machine learning context). During the first phase, the attacker uses a profiling device (which is similar to the target device and on which input parameters as the secret key and plaintext can be set arbitrarily) to build a very precise model of the physical leakage. For that purpose, he acquires a set of S_P side channel traces $\mathbf{x} \in \mathbb{R}^N$ from the profiling device, where N denotes the number of sample points in the measurements. Let $y = g(p, k)$ be a random variable representing the result of an intermediate operation of the target cipher which depends partly on public information p (plaintext or ciphertext chunk) and secret key (byte) $k \in \mathcal{K}$, where \mathcal{K} is the set of possible key values. The value of y is assumed to have an influence on the deterministic part of the power or EM measurements. As a final step, the adversary estimates the probability distribution:

$$\Pr[\mathbf{x}|Y = y] \quad (1)$$

using the profiling set $\mathcal{D}_{Profiling} = \{(\mathbf{x}_i, y_i)\}_{i=1}^{S_P}$.

In the attack phase, a new set \mathcal{D}_{Attack} composed of S_A attack traces from the actual target device is acquired by the adversary. The target device is structurally identical to the profiling device whereby the secret key k is fixed but unknown. In order to recover k , the adversary follows a maximum likelihood strategy and estimates the posterior probability for all possible key candidates k^* using Bayes' theorem:

$$\mathbf{d} = \prod_{i=1}^{S_A} \Pr[Y = y_i | \mathbf{x}_i] = \prod_{i=1}^{S_A} \frac{\Pr[\mathbf{x} = \mathbf{x}_i | y_i = g(p_i, k^*)]}{\Pr[y_i = g(p_i, k^*)]} \quad (2)$$

where the k -th entry in the score vector \mathbf{d} corresponds to the correct key candidate [27].

B. Convolutional Neural Networks (CNNs)

CNNs incorporate dedicated knowledge about a specific type of input into their architecture. They are designed to

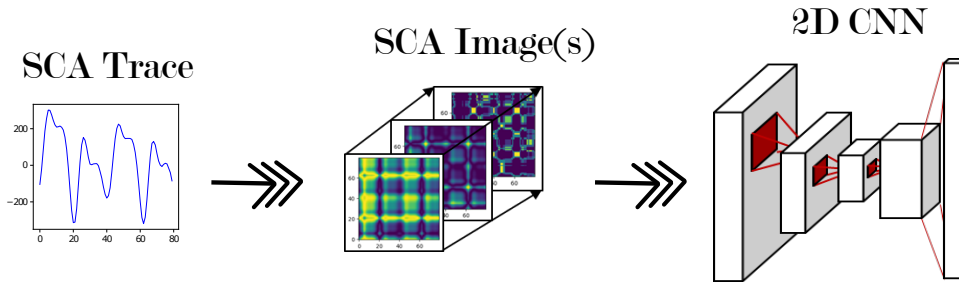


Fig. 1: Top-level overview of our approach. One-dimensional SCA traces are transformed into images, which are later used as input for a 2D CNN. It is also possible to stack several pictures generated from the same trace like different channels in an RGB image.

process data that has a grid like topology such as time-series data or images. Such data usually has a strong local structure meaning that variables (or pixels) that are spatially or temporally nearby are highly correlated [11]. Unlike traditional learning algorithms, CNNs are able to automatically extract and combine local and global features. The main building blocks for that purpose are the *convolution* and *pooling* layers which are introduced in the following subsections. Afterwards, we give a brief overview about the principal architecture and training of CNNs. We refer the reader to [24] for a comprehensive description of CNNs and DL in general.

1) *Convolutional Layer*: This type of layer is the core building block of a CNN to exploit spatially local correlations. To this end, a kernel or filter \mathbf{W} of size $r \times r$ (sometimes called receptive field) glides throughout the input \mathbf{F} of size $m \times m$ and calculates an activation or feature map $\tilde{\mathbf{F}}$ according to the formula:

$$\tilde{\mathbf{F}}(x, y) = \sum_{i=1}^r \sum_{j=1}^r \mathbf{F}(x+i, y+j) \cdot \mathbf{W}(i, j), 1 \leq x, y \leq m \quad (3)$$

There are usually several kernels in a convolutional layer, whereby every kernel creates a corresponding feature map which are stacked together along the depth dimension. The weight parameters of the kernels are learned to activate when they detect a specific feature or pattern in the input.

2) *Pooling Layer*: The pooling layers are responsible to reduce the resolution of the input in order to decrease the number of parameters and the computational complexity of the network. In most CNNs, this is done by the max-pooling operation which considers only the maximum value within a rectangular neighborhood. Apart from downsampling the data stream, pooling helps the network to be invariant to small translations of the input, i.e., the exact location of a structure is not important but if the structure is present in the input at all.

3) *Architecture & Learning*: Typical CNN constructions consist of repetitive blocks of convolution and pooling layers. The basic concepts of sparse, local connectivity, weight sharing and subsampling enable the network to extract more abstract representations of given inputs. On top of the feature extractor part, fully connected layers, which are composed

of neurons as in traditional neural networks, are responsible for feature combination and finally classification of the input. Non-linear activation functions, such as *sigmoid* or *Rectified Linear Unit (ReLU)*, ensure that the network is able to approximate more complex dependencies. These are directly connected to the output of convolutional or fully-connected layers. The neurons in the last layer output class scores in form of a probability distribution by means of the Softmax function.

CNNs are usually trained in an iterative, multi-step process by which the weights of the kernels and neurons are optimized to minimize a dedicated loss function (i.e., the categorical cross-entropy in a classification setting). The loss depicts the difference between the expected output (i.e. labels) and the prediction result produced by the last layer. For faster convergence, gradient-based optimizer algorithms such as *Stochastic Gradient Descent (SGD)* or *ADAM* are applied in practice for updating the parameters of the model. An important hyperparameter that controls the training process is the learning rate, which determines how fast the weights of the network are driven towards the optimal solution.

IV. SIDE-CHANNEL ANALYSIS IN 2D

In this section we introduce our method to create 2D representations of power traces. To that end, we investigate different signal processing techniques and give suitable parameter settings. Afterwards, we compare the methods with respect to the amount of leakage that can be detected in the generated images.

A. Imaging Side-Channel Traces

In the following, we discuss four techniques to transform a vector $\mathbf{x} = [x_1, \dots, x_N] \in \mathbb{R}^N$ consisting of side-channel measurements into a matrix $\mathbf{X} \in \mathbb{R}^{M \times N}$, where M and N denote the height and width of the matrix. An overview of all techniques is provided in Table I. The motivation to encode SCA traces as images is to generate new and more discriminative features that are not directly present in the time domain. This enables us to treat the problem of classifying power traces in a profiled SCA as an image recognition task, which can be effectively handled by 2D CNNs. It is furthermore possible

TABLE I: Overview of transformation techniques into 2D space

	GAF	MTF	RP	STFT
Encoded information	Superposition/Difference of temporal correlations	Transition probabilities between quantiles	Phase space dynamics	Frequency per time
Parameters [used value]	PAA [false]	Number of quantiles Q [8]	Dimension of trajectories M [1], delay τ [1], threshold ϵ [0], binarization [false]	Window type [Hann], window length Δt [8], overlap [0.9· Δt], sample frequency F_S [1.25/2 · 10 ⁹ Hz]
Image size (for trace of length N)	$N \times N$	$N \times N$	$N \times N$	$N \times 5$

to concatenate different 2D representations of a single power trace into a multi-channel image to enhance the robustness and performance of the classifier.

1) *Gramian Angular Field (GAF)*: GAF exploits the temporal correlation of the time series data to create images [14]. For that purpose, a time series trace \mathbf{x} is rescaled to a range of $[-1, 1]$ using a Min-Max scaler:

$$\tilde{x}_i = \frac{x_i - \max(\mathbf{x}) + (x_i - \min(\mathbf{x}))}{\max(\mathbf{x}) - \min(\mathbf{x})} \quad (4)$$

Afterwards, the trace is transformed into the polar coordinate system:

$$\begin{cases} \phi = \arccos(\tilde{x}_i), -1 \leq \tilde{x}_i \leq 1, \tilde{x}_i \in \tilde{\mathbf{x}} \\ r = \frac{t_i}{N}, t_i \in \mathbb{N} \end{cases} \quad (5)$$

The normalization of the trace in (4) and the arccos in (5) result in a bijective mapping in the polar coordinate system. The radius for the calculated value \tilde{x}_i is determined through its point in time t_i in the trace. This is important, because two different traces must not lead to the same image. Thus, the temporal correlations for each measurement are preserved. The last step is to calculate the Gram-Matrix \mathbf{G} using the transformed values:

$$\mathbf{G} = \begin{bmatrix} \cos(\phi_1 + \phi_1) & \dots & \cos(\phi_1 + \phi_N) \\ \cos(\phi_2 + \phi_1) & \dots & \cos(\phi_2 + \phi_N) \\ \vdots & \ddots & \vdots \\ \cos(\phi_N + \phi_1) & \dots & \cos(\phi_N + \phi_N) \end{bmatrix} \quad (6)$$

The usage of angles to create the Gram-Matrix leads to a non-Gaussian distribution. This can be shown, when the trigonometric sum, as defined in (6), is converted to the Cartesian coordinate system:

$$\begin{aligned} \cos(\phi_1 + \phi_2) &= \cos(\arccos(x_1) + \arccos(x_2)) \\ &= \cos(\arccos(x_1)) \cdot \cos(\arccos(x_2)) \\ &\quad - \sin(\arccos(x_1)) \cdot \sin(\arccos(x_2)) \\ &= x_1 \cdot x_2 + \sqrt{1 - x_1^2} \cdot \sqrt{1 - x_2^2} \end{aligned} \quad (7)$$

As shown in (7), a penalty term $\sqrt{1 - x_1^2} \cdot \sqrt{1 - x_2^2}$ is added in the Cartesian system. It reaches its maximum when $x_1 = x_2 = 0$. Another advantage of equation (6) is that the original time series value can be reconstructed through the main diagonal of the matrix.

The GAF comes in two different versions. On the one hand as shown in equation (6), which is known as Gramian Angular

Summation Field (GASF) and on the other hand the Gramian Angular Difference Field (GADF) which is defined as follows:

$$\mathbf{G} = \begin{bmatrix} \sin(\phi_1 - \phi_1) & \dots & \sin(\phi_1 - \phi_N) \\ \sin(\phi_2 - \phi_1) & \dots & \sin(\phi_2 - \phi_N) \\ \vdots & \ddots & \vdots \\ \sin(\phi_N - \phi_1) & \dots & \sin(\phi_N - \phi_N) \end{bmatrix} \quad (8)$$

In contrast to GASF, GADF uses the difference of the values over the time t to calculate the temporal correlation. Moreover, it is not possible to reconstruct the original trace through the main diagonal since:

$$\sin(\phi_i - \phi_i) = 0, i = 1 \dots N \quad (9)$$

The advantage of the transformation to GAF images is that the temporal dependencies are preserved through superposition or differentiation. Additionally, there is no Gaussian distribution anymore which is important for CNNs to ease distinguishing relevant data from noise. However, a disadvantage of those transformations is the increased data overhead. A trace with N sample points results in a $N \times N$ GAF image. In [14], Piecewise Aggregate Approximation (PAA) has been used to reduce the number of data points in time series. We have not applied this step since the averaging induced by PAA would lead to undesired information loss. Instead, we decided to use only parts of the traces for the transformation (details will be explained later in the paper). Examples of GAF images are illustrated in Fig. 2b and Fig. 2c (first row).

2) *Markov Transition Field (MTF)*: This is another time series imaging method introduced by Wang et al. [14]. In order to apply it for SCAs, the power trace \mathbf{x} is divided into Q quantile bins. Every sample point of x_i is assigned to a bin $q_j (j \in [1, Q])$, which segments the data over its amplitude. Subsequently a $Q \times Q$ weighted adjacency matrix \mathbf{W} is created, by counting the transitions between the bins over time using a first-order Markov chain. $w_{i,j}$ represents the frequency by which a point in quantile q_j is followed by a point in quantile q_i . Through the normalization $\sum_j w_{ij} = 1$, the MTF is created. It has the disadvantage that information about the temporal dependencies are lost. Hence, Wang et al. had the idea to define the MTF as follows:

$$\mathbf{M} = \begin{bmatrix} w_{ij|x_1 \in q_i, x_1 \in q_j} & \dots & w_{ij|x_1 \in q_i, x_N \in q_j} \\ w_{ij|x_2 \in q_i, x_1 \in q_j} & \dots & w_{ij|x_2 \in q_i, x_N \in q_j} \\ \vdots & \ddots & \vdots \\ w_{ij|x_N \in q_i, x_1 \in q_j} & \dots & w_{ij|x_N \in q_i, x_N \in q_j} \end{bmatrix} \quad (10)$$

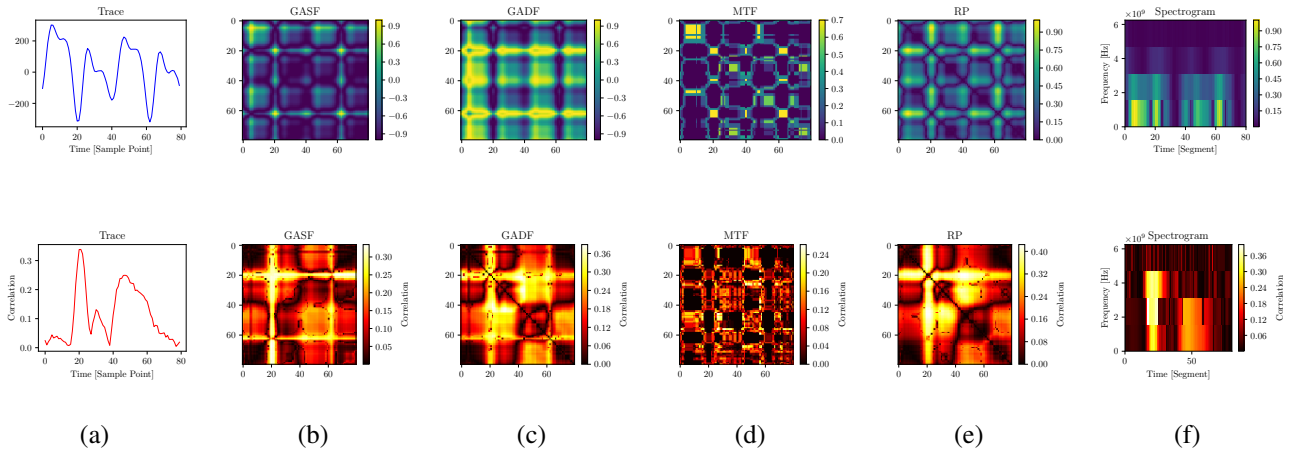


Fig. 2: Images created from power trace the AES-Serial data set: (a) original trace segment, (b) GASF , (c) GADF, (d) MTF, (e) RP, (f) spectrogram. The RP image and the spectrogram have been rescaled into a range between 0 and 1 manually after the transformation. The corresponding correlation plots are shown in the second row.

The quantiles which contain the values x_i and x_j at the time i and j are q_i and q_j ($q \in [1, Q]$). Thus, the MTF M_{ij} represents the transition probability $q_i \rightarrow q_j$. As a result, the MTF shows for each point of time in the trace the probability of the transition from the quantile of the value $x_n \in q_i$ to the quantile of the value $x_m \in q_j$. Moreover, $M_{i,j||i-j|=l}$ represents the transition probability within the time interval l . However, the main diagonal M_{ii} is a special case which shows the probability of a transition to the same quantile with $l = 0$. As a last step, to increase the efficiency of computation and to reduce the image size, an average filter with blurring kernel is applied on non-overlapping rectangles. The result of a MTF transformation is visualized in Fig. 2d.

A crucial parameter in the context of SCA is the number of quantile bins Q used during the quantization. We investigated different values in the range $[5, N]$. Intuitively, a larger value leads to a finer subdivision of the signal which seems to be beneficial to capture small differences in the amplitude. However, we got the best results using eight quantiles.

3) *Recurrence Plots (RPs)*: RPs have already been introduced by Eckmann et al. in 1987 [28]. The main idea is to visualize the M -dimensional phase space trajectory of a non-stationary time series signal as a two-dimensional representation of its recurrences. Informally speaking, an RP indicates at which time instances the trajectory of the signal passes almost the same area in the phase space. It can be mathematically described as:

$$\mathbf{R}_{i,j} = \mathcal{H}(\epsilon - \|\vec{x}_i - \vec{x}_j\|), \vec{x} \in \mathbb{R}^T, i, j = 1 \dots N_T \quad (11)$$

where N_T is the number of considered trajectories \vec{x} , ϵ a threshold distance, $\|\cdot\|$ the (Euclidean) norm, and \mathcal{H} the Heaviside function. A single trajectory is defined by:

$$\vec{x}_i = (x_i, \dots, x_{i+(M-1)\tau}), i = 1, \dots, N - (M - 1)\tau \quad (12)$$

where M is the dimension of the trajectories and τ is the time gap between two back-to-back points of the trajectory. RP constructs a symmetric matrix that relates the distance between states as intensity values (i.e. the smaller the distance, the higher the intensity in the image). Typical high-level patterns that can be found in RPs are referred to as topology and can be separated in the categories *homogeneous*, *periodic*, *drift* and *disrupted*. Due to the oscillating signature of power traces, RPs created from them contain large, recurrent structures as shown in the example in Fig. 2e. We have used a phase space dimension $M = 1$ and time delay $\tau = 1$ throughout the experiments in order to capture fine-granular phase change information in the RPs. The choice of these parameter values is also supported by RP literature [29] and furthermore simplifies the combination with other imaging techniques, since the dimensionality of the resulting RP is the same as for GASF/GADF. Additionally, we skipped the binarization induced by the Heaviside function in equation (11) to avoid information loss.

4) *Short Time Fourier Transform (STFT)*: The Fourier transform decomposes a signal into its frequency components. This is shown by the Discrete Fourier Transform (DFT) in equation (13), where \mathbf{x} is the discrete and $F(\omega)$ the frequency transformed signal.

$$F(\omega) = \sum_{n=0}^{N-1} \mathbf{x}[n] e^{-i \frac{2\pi\omega n}{N}}, \omega = 0, \dots, N - 1 \quad (13)$$

However, by transforming a signal into the frequency domain, time resolution is lost. Thus, it is known that a certain frequency occurred but not when in time. This poses a problem for SCAs, where it is beneficial to know within which time a certain frequency occurs. Therefore, as shown in equation (14), the STFT does not transform the whole signal at once. Instead, a window function $w[n - m]$ is used which slides over the signal $\mathbf{x}[n]$. Only the selected area of the window is

transformed into frequency domain using DFT. By doing so, the frequencies within a time period of Δt are received.

$$STFT(m, \omega) \equiv F(m, \omega) = \sum_{n=-\infty}^{\infty} \mathbf{x}[n]w[n-m]e^{-i\omega n} \quad (14)$$

The spectrogram is a visualization of STFT and plots the intensity of the STFT magnitude over time.

STFT underlies the K upfm uller’s uncertainty principle, which describes a correlation between the resolution of the time and the frequency domain. As a consequence, a high time resolution leads to a blurry resolution in the frequency domain and vice versa. That is because frequencies whose period length is larger than the window size Δt cannot be resolved. In the context of SCAs, Yang et al. suggested to choose window lengths in a range between 64 and 256 to obtain a reasonable frequency resolution and balanced spectrogram image sizes [30]. However, as we will demonstrate in the next section, also smaller window sizes which lead to spectrograms having the same time resolution than the original signal can give promising results. They have just to be adjusted to the special properties of CNNs. An example spectrogram using a window length of 8 is shown in Fig. 2f.

B. Power Leakage Analysis in Images

In order to compare the amount of information that is encoded by the different techniques, we have calculated the Pearson correlation between the generated images and leakage sensitive variable y . For that purpose, we first unrolled the images along the height dimension into 1D arrays. Once the correlation coefficient has been determined for individual pixels, we constructed a 2D matrix of the same size as the images.

The second row of Fig. 2 illustrates the result using 1000 images per technique. One can observe that equivalent structures can be found in the images and corresponding correlations. Bright areas in the correlation plots indicate locations with higher leakage, and areas with low information content are depicted in black. It can be seen that GASF, GADF and RP images show leakage in similar regions in the upper left part, while the leakage in MTF images is more distributed. The leakage in spectrograms is most concentrated due to the small frequency resolution. Another interesting point can be noticed when comparing the highest amplitude of the correlation for the 1D traces (Fig. 2a) with the maximum correlations that can be found in the images. GADFs (≈ 0.38), RPs (≈ 0.42) and spectrograms (≈ 0.38) seem to contain more information than the original traces (≈ 0.33). However, MTF shows a lower correlation maximum (≈ 0.26). The leakage of GASF images is on a similar level as in the traces. From that result, we expect better results for at least some of the imaging techniques compared to SCAs in 1D.

V. EXPERIMENTS

In this section, we investigate the performance of the aforementioned transformation techniques in the context of DL-based SCAs.

TABLE II: Network configuration of CNN

Layer Type	Hyperparameters
Convolution 2D	filters=8, kernel size=5x5, L2-reg=0.01
Batch Normalization	-
Activation	ReLU
Max-Pooling	pool size=2x2, stride=2
Dropout	rate=0.5
Convolution 2D	filters=16, kernel size=3x3, L2-reg=0.01
Batch Normalization	-
Activation	ReLU
Max-Pooling	pool size=2x2, stride=2
Dropout	rate=0.5
Flatten	-
Fully-Connected	neurons=250, activation=ReLU
Batch Normalization	-
Dropout	rate=0.3
Fully-Connected	neurons=256, activation=Softmax

A. CNN Architecture

The CNN architecture we have used throughout all experiments is given in Table II. It consists of two blocks each of which contains a convolution and max-pooling layer followed by two fully-connected layers. Dropout layers and L2-regularization are included for better generalization of the model and help to reduce overfitting [24]. Additionally, batch normalization is applied to establish a stable distribution of activation values, which makes the network more robust to parameter tuning. We have trained the CNN using the Adam optimizer and a learning rate of 0.0002. In order to avoid overfitting, the weights leading to the smallest validation loss has been saved during training, and the process has automatically been stopped once the validation loss has not decreased for 20 consecutive epochs.

Our elaborated network configuration is inspired partly by *VGGNet* [31] which showed remarkable performance in image recognition. However, we are using fewer convolutional blocks and the fully-connected layers are of smaller size since our network only has to discriminate between $2^8 = 256$ different categories (classification of one byte) instead of 1000. We also experimented with a pre-trained feature extractor (convolution and pooling layers) of VGGNet, but got inconsistent results. This is potentially because VGGNet has been trained with real life objects, while our setup requires to classify time-series images which are composed of completely different structures and features. Please note that the goal of our paper is not to describe an optimal network architecture but rather to illustrate the advantages of SCA in 2D domain in general. Nevertheless, our proposed CNN model is able to reach a high performance on all data sets.

B. Data Sets

We consider four different data sets: an unprotected hardware AES, an AES hardware implementation with random jitter, a hardware AES setup with high noise, and a side-channel protected software AES. The size of the profiling and attack sets have been set to $S_P = 50\,000$ and $S_A = 10\,000$ examples for all data sets. We describe them briefly in the following.

1) *Unprotected Hardware AES*: The power traces of this data set originate from an unprotected hardware implementation of the AES running on a ZYNQ UltraScale+ FPGA. The implementation contains a single S-Box instance, which is why we refer to this data set as AES-Serial. It is commonly known that the most leakage in a hardware implementation is caused by register transitions [23]. Therefore, we have used the XOR of two consecutive S-Box outputs in the first round as target operation and consequently as labels for training. A single measurement originally contains 1000 sample points, but we have only used a segment of 80 data points from the traces to generate the images (the location of these points was roughly determined by correlation with known key). Please note that the reduction has only been done in order to speed-up the experiments, we expect similar results using the complete traces.

2) *Hardware AES with desynchronization*: This data set is similar to the former one except that the traces have been artificially desynchronized. To this end, we have shifted each trace to the right with a random offset in the range of $[0, 50]$. Such misalignments can occur due to an unstable measurement setup or a jitter-based countermeasure (e.g. by creating an unstable clock signal [32]). Since CNNs are, to some extent, robust against variations in the input space as explained in Section III-B, our goal is to evaluate the image-based SCA approach under such conditions. We cut out segments of 180 sample points length from the traces for creating the images in order to ensure that enough leakage information is available.

3) *Hardware AES with high noise*: Another range of experiments are based on the public data set of the *DPA Contest v2* [33]. These side-channel traces were acquired from an unprotected AES design running on an FPGA platform. The used AES module performs one round per clock cycle. Each trace contains 3253 sample points and covers a complete encryption operation. We have pre-selected 500 sample points for the experiments in order to attack the last round of the encryption. Several studies noted that this data set is relatively noisy and hard to attack [34].

4) *Protected Software AES*: The last data set we use for the evaluation has been obtained from the public SCA database *ASCAD* [27]. The targeted platform is a first-order secured implementation of the AES running on an 8-bit ATmega8518 microcontroller. Each trace is composed of 700 sample points and the targeted intermediate result is the third byte of the masked S-Box output that is processed during the first round. However, for training of the CNN, we only use the unmasked result of the S-Box as labels to check whether the network is able to learn an higher-order attack using the information encoded in the images. For that purpose, the CNN has to combine the leakages of the masks with the leakages of the masked S-Box. Considering the SNR analysis given in [27], those leakages occur roughly between the sample points 140–240 and 450–550. We therefore only used the respective parts of the traces as input for the 2D transformations and removed the remaining data points.

C. Methodology

After the traces have been encoded as images according to Section IV, the CNN described in Table II has been trained to solve the multi-class classification problem defined in Section III-A. As evaluation metric, we have used the well-known Key Guessing Entropy (KGE) or key rank function. The KGE quantifies the difficulty to retrieve the correct value of the key byte regarding the required number of attack traces [35]. It is calculated by replacing the probabilities on the right-hand side of equation (2) by its approximations retrieved from the CNN, and a ranking of the score vector after the evaluation of each attack trace. Intuitively, the faster the key rank converges to one, the more powerful is the attack. In order to reduce the statistical bias that is induced by the random initialization of the CNN weights, we have trained the network from scratch for ten times. During each run, we performed five independent attacks using 2000 images/traces from \mathcal{D}_{Attack} . Finally, the mean key rank over all ten runs has been calculated which is similar to a ten-fold-cross validation evaluation as defined in [27].

We have implemented our attack framework in Python using the open-source DL framework *Keras* [36]. Training of the CNN has been performed on a single Nvidia Tesla V100 GPU. As a baseline, we also executed the attack using the raw trace segments by replacing the 2D convolution and pooling operations in our CNN with their 1D equivalents. Additionally, we compared our results to three different types of (unsupervised) 1D preprocessing techniques which are widely used in side-channel analysis for comparison: SSA, Fast Fourier Transform (FFT), and PCA using the 15 highest ranked components (this choice of parameter gave the best results in our experiments).

D. Results for Single Image Attacks

Fig. 3 shows the results for the 1D baseline attacks in the first row, and the single image-based attacks in the second row. From there, one can observe the following:

1) *GAF*: The GAF methods show almost similar results in the AES-Serial, AES-Desync and DPA-v2 data sets, while GASF shows a considerably steeper key rank curve than GADF for the protected software AES. We expected a larger difference between the two GAF variants since GASF images encode information about the original power trace in its main diagonal which is not directly present in GADF images. It seems that the temporal correlations contained in GAF images alone provide enough features to recover the secret key. Another notable point is the good performance on the desynchronized data set. While the remaining transformation techniques and also the 1D attacks need more traces to reach a key rank of 1 compared to the aligned traces, GASF and GADF show a better KGE. This can be explained by the representation of the 1D signal in polar coordinates, which helps to preserve absolute temporal relations. Additionally, the spatial diversity of features in GAF images provide a regularization factor that is known from data augmentation methods. This improves the CNN model’s ability to generalize distortions in the test set. We will exploit this aspect later in

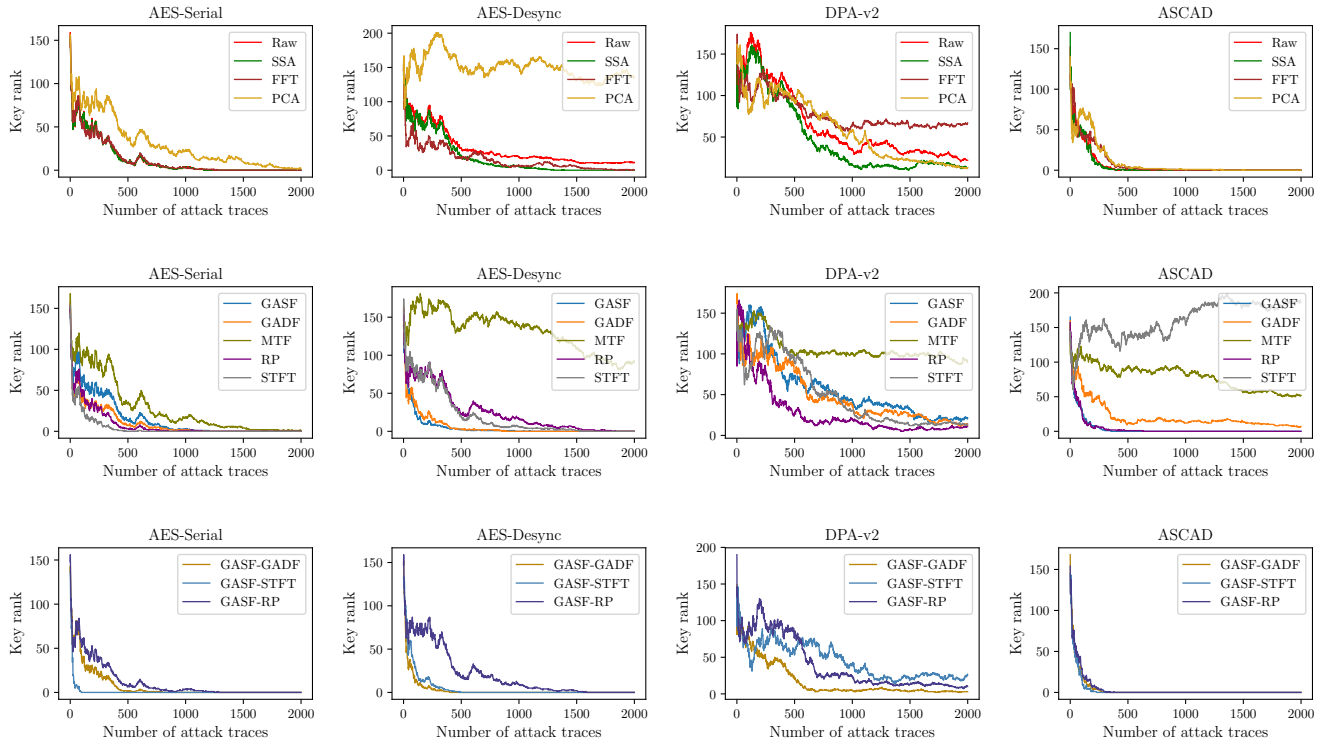


Fig. 3: Overview of attack results over the four data sets. The mean KGE for the 1D baseline (raw traces) along with the 1D transformation methods are illustrated in the first row. The second row shows the mean key ranks for the single image attacks, while the combined image attack results are illustrated in the third row.

the paper to further enhance the performance of GAF-based attacks.

2) *RP*: The RP transform performs best in two out of the four data sets among the image-based attacks, and is able to consistently beat the 1D baseline. Except for the AES-Desync data set, it furthermore performs similar or better than the best 1D preprocessing method SSA. This proves that recurrence as defined in equation (11) is a suitable method to represent variations in the power consumption, which can be exploited effectively by a 2D CNN to distinguish between different values of the attacked operation.

3) *MTF*: Looking at the result for MTF, one can see that it has a significantly worse key rank than the other approaches in all four data sets. One reason is the reduction of temporal dependencies through the quantization step, which is required for building the transition matrix. Another reason is that the MTF transform produces a non-bijective mapping, i.e., reconstructing the raw trace from an MTF image in an accurate manner is - in contrast to GAF - hardly possible. However, previous work showed that this property is an important factor for classifying time series images. The observation that GAF generally performs superior to MTF is thus in line with other published results [14] and our correlation analysis shown before.

4) *STFT*: The best performance on the AES-Serial data set is achieved by the STFT-based attack. Although the

spectrograms only contain five frequency bands, the additional information helps to reduce the amount of required attack traces from 1000 to 500 in order to achieve a KGE of one compared to the 1D baseline attacks. An improved KGE can also be reported for the desynchronized AES traces and the noisy DPA-v2 data set. However, the spectrogram-CNN fails to attack the first-order secured implementation. We initially assumed that a window length of eight in STFT may result in a too small frequency resolution for the ASCAD data set, as the traces have been sampled with a rate of 2 GS/s. However, we got almost the same result when using larger STFT window sizes (16, 64, 96, 128) following the guidelines of Yang et al. [30]. We will later see that not the STFT parameters are the reason for the bad performance, but the way how the spectrogram is given to the CNN.

E. Results for Combined Image Attacks

The transformation techniques presented above encode different types of information about time series data (like power measurements): GASF/GADF show the superposition/difference of directions at two time steps, MTF images encode transition probabilities from quantile to quantile, RPs reveal space dynamics as distance between corresponding trajectories, and spectrograms visualize the energy of a signal as a function of frequency and time. Thus, we can consider them as complementary representations of the same data

source which can be combined into a single image to improve the classification performance of the CNN. The combination has been done by concatenating images generated from the corresponding power trace along the z-axis as shown in the center of Fig. 1. Except for spectrograms, this was easily possible since the images are of identical vertical and horizontal resolution. To join spectrograms with other images, we have upsampled the y-axis by dividing the five frequency bands until the proper resolution has been reached (i.e. a rectangular shape).

We have concentrated our evaluation on GASF- X combinations due to the good performance of GASF on single image attacks. The results are illustrated in the third row of Fig. 3. From there, one can notice the following:

1) *GASF-RP*: This combination yields a small enhancement of the KGE in the attack against the protected software AES, likely because both techniques individually perform well on this data set. The results on the other data sets are comparable or even worse than single image RP attacks. This indicates that RP and GASF features are too diverse for the early data fusion approach that we have applied in this work. The analysis of a combination of RP and GASF features in a deeper CNN layer (i.e. late information fusion [37]) is subject to future work.

2) *GASF-STFT*: The setup of rescaled spectrograms and GASF images shows the best KGE in two out of four data sets. The margin to the remaining methods is especially large in the AES-Serial data, where a stable key rank of one is reached with less than 100 attempts. This means an improvement of a factor of ten compared to the 1D baseline and single GASF, and a factor of five compared to unscaled spectrograms. The performance increase for the ASCAD data set is also remarkable considering the worse result of the spectrogram-only attack. We found that this mismatch is mainly due to the frequency upscaling of spectrograms needed for the image fusion. It improves the CNN kernel’s ability to capture transitions between different frequency bands. While in the unscaled spectrograms all frequency bands have been processed together by the kernel in the first layer, in the upsampled variant at most two frequency bands are evaluated in parallel. This enables the kernels to create more discriminant and informative features for deeper layers. Indeed we could examine that the scaled spectrograms alone give a significantly improved KGE compared to the unscaled version, and also with regard to spectrograms having a higher frequency resolution that were generated with a larger STFT window parameter. However, similar to GASF-RP images, there seems to be no improvement on the DPA-v2 data set. These findings suggest that a concatenation of different image types is of less benefit in case of highly noisy setups.

3) *GASF-GADF*: The combination of the GAF images shows remarkable results for the AES-Desync and DPA-v2 data sets. This makes it very suitable for attacks on misaligned and noisy traces. The combination is the only one which could improve the KGE over all data sets compared to single image attacks. furthermore, GASF-GADF is the only combination

TABLE III: Comparison of attacks for the ASCAD data set

Source	KGE ≤ 2	Evaluation Method
[27]	≈ 450	10-fold-cross validation
[10]	≈ 500	Repeated random subsampling
[38]	≈ 700	10-fold-cross validation
[39]	338	Mean rank (mask values revealed)
This Paper	≈ 275	10-fold-cross validation

that is able to perform better than the 1D-based attacks in all setups. The GAF transformations have different representations of temporal relations which rely on polar coordinates. Therefore, it seems that the CNN is able to detect features in the combined representations of temporal correlations to enhance the classification accuracy for all attacked data sets.

In order to compare the results of the combined GASF-GADF attack with other work, we show the KGE of related approaches in Table III. We focus the comparison on the ASCAD database since it represents a de-facto benchmark for DL-based SCAs. Although the approaches are not completely comparable due to changing evaluation setups, one can still notice that the image combination attack requires significantly less traces to approach a stable key rank smaller than two. This further motivates the applicability of our approach despite the timing overhead that is introduced through the transformation of the traces into images (i.e. training time per epoch is roughly doubled on our setup compared to the 1D attacks against ASCAD).

F. Image-based Data Augmentation

Data augmentation can be seen as a way to artificially increase the training set by showing the model many variations of the same input data during training. It is an extensively used technique in object classification due to the manifold possibilities to apply geometric modifications to images. The augmentation techniques do not change the label of an image, hence allow the model to better generalize [24]. This section aims to evaluate if 2D representations of power traces can also benefit from image-based data augmentation, especially in cases where the size of the profiling set is rather small. For that purpose, we have restricted the number of training data to $S_P = 1000$, and applied the following five image preprocessing techniques:

- Random rotation by up to 40 degrees, plus a shearing operation with intensity 0.5
- Random horizontal and vertical shift by up to 20% of the image size
- Erasing randomly picked rectangular patches (pixels are set to random values between 0 and 1)
- Gaussian blurring
- Random addition of salt and pepper noise (i.e. individual pixels are set to either zero or one)

The methods have been selected since they represent different classes of augmentation types (geometric and arithmetic operations, segmentation, blurring). We have individually evaluated the effect of each augmentation technique on all kinds of im-

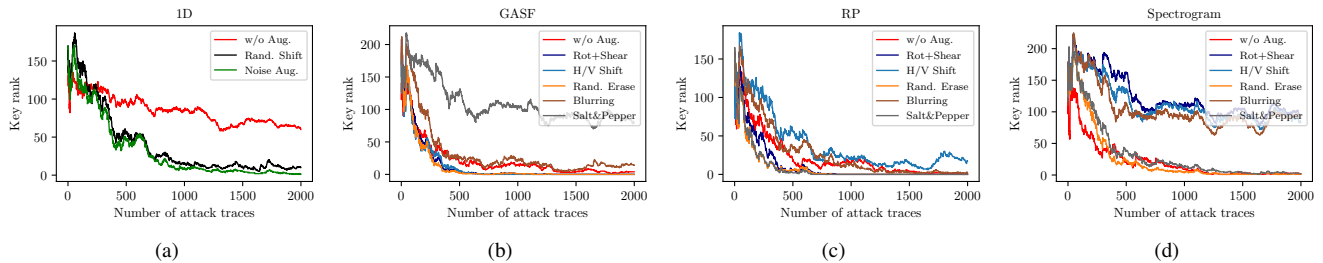


Fig. 4: Comparison of trace- and image-based data augmentation methods using $S_P = 1000$ training examples: (a) 1D Trace, (b) GASF, (c) RP, (d) Spectrogram. The red curves in the plots correspond to attacks without augmentation.

age transformations except MTF (due to the reasons discussed earlier in the paper). Additionally, we have implemented the random shift technique proposed in [8] and the noise addition method of Kim et al. [10] to compare our results with state-of-the-art 1D augmentation techniques. The results are shown in Fig. 4. From there, it can be observed that the augmentation methods perform differently on the imaging types. For example, the geometric operations (rotation, shifting) lead to good results when applied to GASF images, but deteriorate the key rank of spectrogram-based attacks. This can be explained by the usage of polar coordinates in GASF images. Our spectrograms have a very low frequency resolution, thus shifting or rotating introduces too much variance in the training set. Random erasing, on the other hand, gives a notable performance boost in all attacks and seems to be a suitable standard choice. It introduces an explicit form of regularization by adding block noise, but maintains the global structure of the image. This feature already showed good results on various recognition tasks [40].

When comparing image-based augmentation with trace-based augmentation, one can easily notice that image-based augmentation is superior. While the 1D attacks only manage a key rank between 15 and 20 using 2000 encryptions, some of the GASF and RP-based attacks have a stable KGE below two with only 700 traces. This means, by using image augmentation, we achieved better results in the GASF and RP-based attacks than in the experiments of Section V-D with only 1/50 of the training set. Another interesting point to notice is the large gap between the curves without augmentation. The imaging methods are still able to converge to a rank below five, while the 1D attack reaches a key rank of around 60 after 2000 attempts. This is an unexpected result as the 2D CNN has ten times the amount of trainable parameters compared to the 1D version. Thus, the 2D model is much more prone to overfitting in our restricted setting with only 1000 training samples. However, the 2D attacks still outperform the 1D attacks (even with trace augmentation). Overall, the results of this section clearly confirm the effectiveness of DL-based SCAs in two-dimensional space and the increased information content of the generated images.

VI. CONCLUSION

In this work, we have examined several transformations of 1D power traces into a 2D space in order to improve the efficiency of DL-based SCAs. The performance has been evaluated against advanced 1D representation techniques using four different data sets. Among the considered methods, GAF and RP have shown the best results in single image attacks. Furthermore, we have compared different combinations of images, which resulted in a further enhancement of the classification. The combination of GASF-STFT has shown a tenfold improvement on the AES-Serial implementation over the 1D baseline, and GASF-GADF has proven remarkable results on both desynchronized and noisy AES traces. These two combinations have demonstrated very robust results on all data sets and outperform related approaches on the public ASCAD database. Finally, we have investigated the impact of data augmentation on the transformed traces, and were able to observe the superiority of imaging methods over state-of-the-art 1D attacks.

As a future work, we intend to evaluate other types of data augmentation techniques, as well as a combination of different techniques. Another interesting path could be to explore the effect of image feature fusion in a deeper layer of the DNN, instead of the image stacking approach we have applied in this work. We expect these methods to further improve the promising results of this paper.

VII. ACKNOWLEDGMENT

This work is supported in parts by the German Federal Ministry of Education and Research (BMBF) under grant agreement number 16KIS0606K (Security by Reconfiguration - SecRec)

REFERENCES

- [1] P. C. Kocher, "Timing attacks on implementations of diffie-hellman, rsa, dss, and other systems," in *Proceedings of the 16th Annual International Cryptology Conference on Advances in Cryptology*, ser. CRYPTO '96. London, UK, UK: Springer-Verlag, 1996, pp. 104–113. [Online]. Available: <http://dl.acm.org/citation.cfm?id=646761.706156>
- [2] E. Brier, C. Clavier, and F. Olivier, "Correlation power analysis with a leakage model," in *Cryptographic Hardware and Embedded Systems - CHES 2004: 6th International Workshop Cambridge, MA, USA, August 11-13, 2004. Proceedings*, M. Joye and J.-J. Quisquater, Eds. Berlin, Heidelberg: Springer Berlin Heidelberg, 2004, pp. 16–29.

- [3] B. Gierlichs, L. Batina, P. Tuyls, and B. Preneel, "Mutual information analysis," in *Cryptographic Hardware and Embedded Systems – CHES 2008*, E. Oswald and P. Rohatgi, Eds. Berlin, Heidelberg: Springer Berlin Heidelberg, 2008, pp. 426–442.
- [4] S. Chari, J. R. Rao, and P. Rohatgi, *Template Attacks*. Berlin, Heidelberg: Springer Berlin Heidelberg, 2003, pp. 13–28.
- [5] W. Schindler, K. Lemke, and C. Paar, *A Stochastic Model for Differential Side Channel Cryptanalysis*. Berlin, Heidelberg: Springer Berlin Heidelberg, 2005, pp. 30–46.
- [6] B. Hettwer, S. Gehrler, and T. Güneysu, "Applications of machine learning techniques in side-channel attacks: a survey," *Journal of Cryptographic Engineering*, Apr 2019. [Online]. Available: <https://doi.org/10.1007/s13389-019-00212-8>
- [7] H. Maghrebi, T. Portigliatti, and E. Prouff, "Breaking cryptographic implementations using deep learning techniques," in *Security, Privacy, and Applied Cryptography Engineering: 6th International Conference, SPACE 2016, Hyderabad, India, December 14-18, 2016, Proceedings*, C. Carlet, M. A. Hasan, and V. Saraswat, Eds. Cham: Springer International Publishing, 2016, pp. 3–26.
- [8] E. Cagli, C. Dumas, and E. Prouff, *Convolutional Neural Networks with Data Augmentation Against Jitter-Based Countermeasures*. Cham: Springer International Publishing, 2017, pp. 45–68.
- [9] B. Hettwer, S. Gehrler, and T. Güneysu, "Profiled power analysis attacks using convolutional neural networks with domain knowledge," in *Selected Areas in Cryptography - SAC 2018 - 25th International Conference, Calgary, AB, Canada, August 15-17, 2018, Revised Selected Papers*, 2018, pp. 479–498. [Online]. Available: https://doi.org/10.1007/978-3-030-10970-7_22
- [10] J. Kim, S. Picek, A. Heuser, S. Bhasin, and A. Hanjalic, "Make some noise. unleashing the power of convolutional neural networks for profiled side-channel analysis," *IACR Transactions on Cryptographic Hardware and Embedded Systems*, vol. 2019, no. 3, pp. 148–179, May 2019. [Online]. Available: <https://tches.iacr.org/index.php/TCHES/article/view/8292>
- [11] Y. Lecun, L. Bottou, Y. Bengio, and P. Haffner, "Gradient-based learning applied to document recognition," *Proceedings of the IEEE*, vol. 86, no. 11, pp. 2278–2324, Nov 1998.
- [12] J. D. Nima Hatami, Yann Gavet, "Classification of time-series images using deep convolutional neural networks," 2018. [Online]. Available: <https://doi.org/10.1117/12.2309486>
- [13] Y. M. Costa, L. S. Oliveira, and C. N. Silla, "An evaluation of convolutional neural networks for music classification using spectrograms," *Applied Soft Computing*, vol. 52, pp. 28 – 38, 2017. [Online]. Available: <http://www.sciencedirect.com/science/article/pii/S1568494616306421>
- [14] Z. Wang and T. Oates, "Imaging Time-Series to Improve Classification and Imputation," *arXiv e-prints*, p. arXiv:1506.00327, May 2015.
- [15] S. Merino Del Pozo and F.-X. Standaert, "Blind source separation from single measurements using singular spectrum analysis," in *Cryptographic Hardware and Embedded Systems – CHES 2015*, T. Güneysu and H. Handschuh, Eds. Berlin, Heidelberg: Springer Berlin Heidelberg, 2015, pp. 42–59.
- [16] Y. Souissi, S. Guilley, J. Danger, S. Mekki, and G. Duc, "Improvement of power analysis attacks using kalman filter," in *2010 IEEE International Conference on Acoustics, Speech and Signal Processing*, March 2010, pp. 1778–1781.
- [17] T. Le, J. Clediere, C. Serviere, and J. Lacoume, "Noise reduction in side channel attack using fourth-order cumulant," *IEEE Transactions on Information Forensics and Security*, vol. 2, no. 4, pp. 710–720, Dec 2007.
- [18] W. Liu, L. Wu, X. Zhang, and A. Wang, "Wavelet-based noise reduction in power analysis attack," in *2014 Tenth International Conference on Computational Intelligence and Security*, Nov 2014, pp. 405–409.
- [19] Y. Cao, Y. Zhou, H. Zhang, and W. Yang, "Hilbert transform based vertical preprocessing for side-channel analysis," in *2016 25th International Conference on Computer Communication and Networks (ICCCN)*, Aug 2016, pp. 1–7.
- [20] H. Maghrebi and E. Prouff, "On the use of independent component analysis to denoise side-channel measurements," in *Constructive Side-Channel Analysis and Secure Design*, J. Fan and B. Gierlichs, Eds. Cham: Springer International Publishing, 2018, pp. 61–81.
- [21] B. Gierlichs, K. Lemke-Rust, and C. Paar, "Templates vs. stochastic methods," in *Cryptographic Hardware and Embedded Systems - CHES 2006*, L. Goubin and M. Matsui, Eds. Berlin, Heidelberg: Springer Berlin Heidelberg, 2006, pp. 15–29.
- [22] C. Archambeau, E. Peeters, F. X. Standaert, and J. J. Quisquater, "Template attacks in principal subspaces," in *Cryptographic Hardware and Embedded Systems - CHES 2006*, L. Goubin and M. Matsui, Eds. Berlin, Heidelberg: Springer Berlin Heidelberg, 2006, pp. 1–14.
- [23] S. Mangard, E. Oswald, and T. Popp, *Power Analysis Attacks: Revealing the Secrets of Smart Cards*, 1st ed. Springer Publishing Company, Incorporated, 2010.
- [24] I. Goodfellow, Y. Bengio, and A. Courville, *Deep Learning*. MIT Press, 2016, <http://www.deeplearningbook.org>.
- [25] L. Taylor and G. Nitschke, "Improving Deep Learning using Generic Data Augmentation," *arXiv e-prints*, p. arXiv:1708.06020, Aug 2017.
- [26] S. Pu, Y. Yu, W. Wang, Z. Guo, J. Liu, D. Gu, L. Wang, and J. Gan, "Trace augmentation: What can be done even before preprocessing in a profiled sca?" in *Smart Card Research and Advanced Applications*, T. Eisenbarth and Y. Teglina, Eds. Cham: Springer International Publishing, 2018, pp. 232–247.
- [27] E. Prouff, R. Strullu, R. Benadjila, E. Cagli, and C. Dumas, "Study of deep learning techniques for side-channel analysis and introduction to ascad database," *Cryptology ePrint Archive*, Report 2018/053, 2018, <https://eprint.iacr.org/2018/053>.
- [28] J.-P. Eckmann, S. O. Kamphorst, and D. Ruelle, "Recurrence plots of dynamical systems," *Europhysics Letters (EPL)*, vol. 4, no. 9, pp. 973–977, nov 1987.
- [29] J. S. Iwanski and E. Bradley, "Recurrence plots of experimental data: To embed or not to embed?" *Chaos: An Interdisciplinary Journal of Nonlinear Science*, vol. 8, no. 4, pp. 861–871, 1998. [Online]. Available: <https://doi.org/10.1063/1.166372>
- [30] G. Yang, H. Li, J. Ming, and Y. Zhou, "Convolutional neural network based side-channel attacks in time-frequency representations," in *Smart Card Research and Advanced Applications*, B. Bilgin and J.-B. Fischer, Eds. Cham: Springer International Publishing, 2019, pp. 1–17.
- [31] K. Simonyan and A. Zisserman, "Very deep convolutional networks for large-scale image recognition," 2014, cite arxiv:1409.1556. [Online]. Available: <http://arxiv.org/abs/1409.1556>
- [32] T. Güneysu and A. Moradi, "Generic side-channel countermeasures for reconfigurable devices," in *Cryptographic Hardware and Embedded Systems – CHES 2011*, B. Preneel and T. Takagi, Eds. Berlin, Heidelberg: Springer Berlin Heidelberg, 2011, pp. 33–48.
- [33] TELECOM ParisTech SEN research group, "DPA Contest v2." [Online]. Available: <http://www.dpacontest.org/v2/>
- [34] S. Picek, I. P. Samiotis, A. Heuser, J. Kim, S. Bhasin, and A. Legay, "On the performance of convolutional neural networks for side-channel analysis," *Cryptology ePrint Archive*, Report 2018/004, 2018, <https://eprint.iacr.org/2018/004>.
- [35] F.-X. Standaert, T. G. Malkin, and M. Yung, "A unified framework for the analysis of side-channel key recovery attacks," in *Advances in Cryptology - EUROCRYPT 2009*, A. Joux, Ed. Berlin, Heidelberg: Springer Berlin Heidelberg, 2009, pp. 443–461.
- [36] "Keras Documentation." [Online]. Available: <https://keras.io/>
- [37] A. Eitel, J. T. Springenberg, L. Spinello, M. Riedmiller, and W. Burgard, "Multimodal Deep Learning for Robust RGB-D Object Recognition," *arXiv e-prints*, p. arXiv:1507.06821, Jul 2015.
- [38] P. Robyns, P. Quax, and W. Lamotte, "Improving cema using correlation optimization," *IACR Transactions on Cryptographic Hardware and Embedded Systems*, vol. 2019, no. 1, pp. 1–24, Nov. 2018. [Online]. Available: <https://tches.iacr.org/index.php/TCHES/article/view/7332>
- [39] C. Pfeifer and P. Haddad, "Spread: a new layer for profiled deep-learning side-channel attacks," *Cryptology ePrint Archive*, Report 2018/880, 2018, <https://eprint.iacr.org/2018/880>.
- [40] Z. Zhong, L. Zheng, G. Kang, S. Li, and Y. Yang, "Random Erasing Data Augmentation," *arXiv e-prints*, p. arXiv:1708.04896, Aug 2017.